RESEARCH ARTICLE

NANO · MICRO small
www.small-journal.com

Modulation of Hydrogen Desorption Capability of Ruthenium Nanoparticles via Electronic Metal-Support Interactions for Enhanced Hydrogen Production in Alkaline Seawater

Junwei Sun, Zhichao Wang, Yue Wang, Yanyan Song, Yi Pei, Wensheng Yan, Rui Xiong, Yan Liu, Bin Lin, Xin Wang, Xiaoyan Zhang, Junfeng Chen,* and Lixue Zhang**

The development of efficient and stable electrocatalysts for the hydrogen evolution reaction (HER) is essential for the realization of effective hydrogen production via seawater electrolysis. Herein, the study has developed a simple method that combines electrospinning with subsequent thermal shock technology to effectively disperse ruthenium nanoparticles onto highly conductive titanium carbide nanofibers (Ru@TiC). The electronic metal-support interactions (EMSI) resulted from charge redistribution at the interface between the Ru nanoparticles and the TiC support can optimize hydrogen desorption kinetics of Ru sites and induce the hydrogen spillover phenomenon, thereby improving hydrogen evolution. As a result, the Ru@TiC catalyst exhibits outstanding HER activity, requiring low overpotentials of only 65 mV in alkaline seawater at the current density of 100 mA cm^{-2}. Meanwhile, Ru@TiC demonstrates excellent stability, maintaining consistent operation at 500 mA cm^{-2} for at least 250 hours. Additionally, an anion exchange membrane electrolyzer incorporating Ru@TiC operated continuously for over 500 hours at 200 mA cm^{-2} in alkaline seawater. This study highlights the significant potential of robust TiC supports in the fabrication of efficient and enduring electrocatalysts that enhance hydrogen production in complex seawater environments.

1. Introduction

Amid the depletion of fossil fuels and escalating environmental challenges, the pursuit of carbon neutrality has become increasingly crucial in energy engineering, where hydrogen (H_2) attracts significant attention for its zero carbon emissions and high gravimetric energy density.[1,2] Producing pure hydrogen through electrochemical water splitting is regarded as the most promising green and cost-effective method.[3–5] Currently, commercial electrocatalytic hydrogen production relies on high-purity water, but freshwater scarcity and purification costs hinder the widespread adoption of electrochemical water splitting technology.[6,7] To address these issues, the direct electrolysis of seawater, particularly under alkaline conditions, has garnered substantial interest within the scientific community.[3,8–10] Nonetheless, a significant challenge in alkaline seawater electrolysis is catalyst corrosion induced by chloride ions (Cl^-), which can markedly affect the durability of electrocatalysts.[11,12] In addition, the slow reaction kinetics stemming from the limited availability of protons for the hydrogen evolution reaction (HER) process is another bottleneck that hinders the progress of alkaline seawater splitting.[13,14] Consequently, designing corrosion-resistant electrocatalysts to accelerate HER kinetics is imperative.

Ru-based electrocatalysts have garnered enormous attention for HER owing to their economic viability, favorable water dissociation capabilities, and platinum-like electrocatalytic water splitting performance.[15–17] Unfortunately, the strong Ru-H bonds significantly influence the hydrogen desorption capacity of Ru-based catalysts, which consequently results in sluggish reaction kinetics of HER.[18–20] Accordingly, a variety of strategies have been implemented to optimize the strength of Ru-H bonds, encompassing the incorporation of a secondary element,[19] the ligand effect induced by surface modification,[21,22] and the adjustment of support materials.[20] Especially, metal-support interactions (MSI) stand out as an effective strategy for tuning the electronic structure and optimizing the electrochemical

J. Sun, R. Xiong, Y. Liu, B. Lin, J. Chen
College of Materials Science and Engineering
Fuzhou University
Fuzhou 350108, P. R. China
E-mail: chenjunfeng@fzu.edu.cn
J. Sun, Z. Wang, Y. Wang, Y. Song, X. Wang, X. Zhang, L. Zhang
College of Chemistry and Chemical Engineering
Qingdao University
Qingdao 266071, P. R. China
E-mail: xyzhang@qdu.edu.cn; zhanglx@qdu.edu.cn
Y. Pei
BNU-HKUST Laboratory of Green Innovation
Advanced Institute of Natural Sciences
Beijing Normal University at Zhuhai
Zhuhai 519087, P. R. China
W. Yan
National Synchrotron Radiation Laboratory
University of Science and Technology of China
Hefei 230026, P. R. China

The ORCID identification number(s) for the author(s) of this article can be found under https://doi.org/10.1002/smll.202411975

DOI: 10.1002/smll.202411975

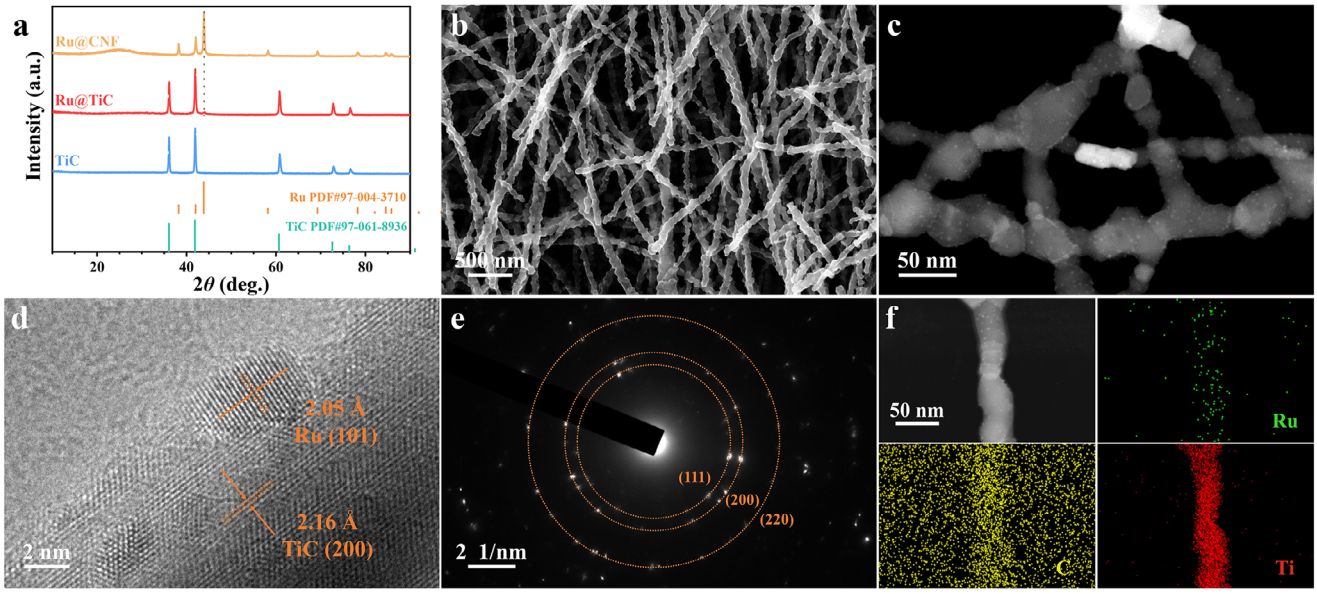

Figure 1. a) XRD patterns of TiC, Ru@TiC, and Ru@CNF. b) SEM, c) HAADF-STEM, d) HR-TEM, and e) SAED images of Ru@TiC. f) The corresponding elemental mapping images of Ru@TiC.

adsorption-desorption intrinsic characteristic at the metal-support interface, thereby enhancing the catalytic performance.[23,24] Carbon-based materials are commonly used as supports for noble metal nanoparticles due to their high specific surface area and excellent electrical conductivity.[22,25,26] However, the carbon corrosion phenomenon and weak interaction between carbon and metal nanoparticles causes the migration of the nanoparticles across the carbon surface during the HER, rendering the composite susceptible to degradation through particle detachment, agglomeration or coalescence, especially in an alkaline electrolyte.[25,27,28] As a consequence, exploiting non-carbon-based supports to anchor Ru sites and modulate its electronic structure is of vital importance to realize enhanced HER catalytic performances under harsh electrolyte environment.

Recently, a wide range of supported catalysts with electronic metal-support interactions (EMSI), induced by charge redistribution on the metal-support heterointerface, have been extensively developed for effective hydrogen evolution.[23,29,30] In particular, transition metal carbides (TMCs)[31,32] with tunable structure, high electrical conductivity, and considerable chemical stability have been cognizant as promising supports to trigger EMSI effects. Among these, TiC has garnered particular interest due to its exceptional properties, including robust corrosion resistance in seawater and strong interaction with noble metals.[33,34] In this study, we develop a simple electrospinning and the subsequently thermal shock technology to disperse Ru nanoparticles (NPs) on highly conductive TiC nanofibers (denoted as Ru@TiC), which induces EMSI between Ru NPs and TiC support. The interactions induced by charge redistribution on the Ru NPs and the TiC support interface can optimize the hydrogen desorption kinetics of Ru sites and trigger the hydrogen spillover phenomenon, thus enhance hydrogen evolution. As a consequence, the as-prepared Ru@TiC exhibits outstanding HER activity in alkaline conditions, requiring overpotentials of only 65 mV to reach the current density of 100 mA cm^{-2} in alkaline seawater. Ru@TiC also achieves considerable electrochemical stability for at least 250 hours at 500 mA cm^{-2}. Notably, an anion exchange membrane (AEM) electrolyzer assembled with Ru@TiC demonstrates excellent stability, with negligible decay within 500 hours in alkaline seawater. This research demonstrates new insight for the development of effective and durable supported HER electrocatalysts and paves the way for the design of energy conversion devices through electronic metal-support interaction.

2. Results and Discussion

2.1. Characteristics of Ru@TiC

Figure S1 (Supporting Information) illustrates the synthetic scheme of Ru@TiC electrocatalyst, which involves the preparation of TiC nanofibers and the subsequent Ru loading procedure via thermal shock process. TiC nanofiber support was initially synthesized using the electrospinning technique and the carburization process. To investigate the interactions between Ru NPs and TiC supports, carbon nanofibers (donated as CNF) and CNF anchored Ru nanoparticles (donated as Ru@CNF) were also prepared accordingly. **Figure 1**a shows the X-ray diffraction (XRD) patterns of the prepared samples. For Ru@TiC, the peaks at 35.9°, 41.7°, 60.5°, 72.5°, and 76.3° correspond to the (111), (200), (220), (311), and (222) of cubic TiC phase (JCPDS No. 97-061-8936), respectively. The weak diffraction peak at 44.0° can be assigned to the (101) plane of metallic Ru (JCPDS No. 97-004-3710), indicating the presence and the low content of Ru species in Ru@TiC sample. Figure S2 (Supporting Information) illustrates the scanning electron microscopy (SEM) images of the as-electrospinning TiC nanofibers precursor, which displays a smooth surface and uniform diameter. SEM images of the CNF precursor also display the smooth surface and a uniform size distribution of diameters (Figure S3, Supporting Information).

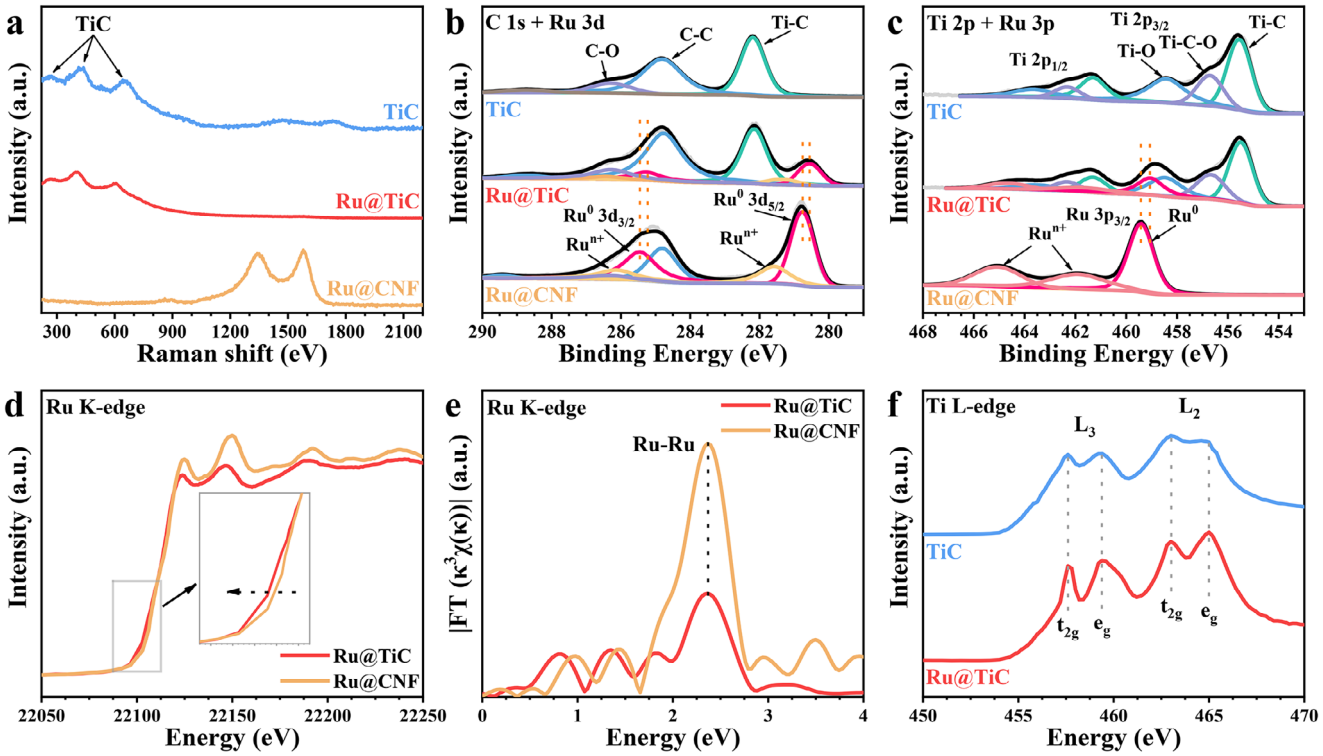

Figure 2. a) Raman spectra of TiC, Ru@TiC, and Ru@CNF. High-resolution XPS spectra of TiC, Ru@TiC, and Ru@CNF in the b) C 1s, Ru 3d, and c) Ti 2p, Ru 3p regions. Ru K-edge d) XANES and e) FT-EXAFS spectra of Ru@TiC and Ru@CNF. f) Ti L-edge XANES spectra of Ru@TiC and TiC.

After the subsequent annealing treatment in Ar atmosphere, TiC nanofiber mat can be obtained. As shown in Figure S4 (Supporting Information), the digital photograph of the self-supporting TiC nanofiber mat reveals its macroscopic morphology as a bulk structure with a deep gray color. TiC nanofibers show the uniformly distributed nanofibers morphology with diameters ranging from 40 to 100 nm (Figure S5, Supporting Information). The roughened surface suggests significant carbon consumption during the carbonization process, leading to a highly carbonized product. In contrast, CNF still maintains the relatively smooth surface after high-temperature carbonization with the diameter being ≈150 nm (Figure S6, Supporting Information).

After completing the thermal shock loading of Ru, Ru@TiC was obtained. As illustrated in Figure 1b, Ru@TiC shows the uniformly distributed nanofibers morphology with no discernible aggregation. High-angle annular dark-field scanning transmission electron microscopy (HAADF-STEM) image indicates the uniform dispersion of Ru NPs on the TiC nanofiber support, as shown in Figure 1c. Importantly, TiC support exhibits a bamboo node-like structure, because of the significant consumption of the carbon component during the carbonization process. As shown in high-resolution transmission electron microscopy (HR-TEM) image of the Ru@TiC in Figure 1d, the characteristic fringe spacings of 0.216 nm can be attributed to the (200) lattice planes of TiC, while the 0.205 nm spacing corresponds to the (101) diffraction plane of Ru. The size of Ru NPs loaded on the support is ≈3.5 nm (Figure S7, Supporting Information). Meanwhile, the (111), (200), and (220) planes in the selected area electron diffraction (SAED) pattern can also be ascribed to TiC phase (Figure 1e). It is noteworthy that diffraction ring characteristic of metallic Ru cannot be detected, which may be correlated with the low content of the Ru species. The elemental mapping images display an even distribution of Ru, Ti, and C elements at the whole Ru@TiC nanofibers, as depicted in Figure 1f. The aforementioned data confirm the uniform dispersion of Ru NPs on the TiC nanofiber support. Nevertheless, Ru NPs aggregate to larger size in the as-prepared Ru@CNF catalyst with an average diameter of ≈8.9 nm (Figure S8, Supporting Information), implying that the metal-support interactions between Ru NPs and TiC support are more pronounced than that of carbon-based support.[25,35–37]

Raman spectroscopy was employed to analyze the local structural changes before and after the thermal shock treatment. As illustrated in **Figure 2**a, the distinct peaks located at 266, 405, and 603 cm^{-1} can be ascribed to the TiC phase,[38–41] signifying that the TiC structure is preserved following the deposition of Ru. Furthermore, the very weakened D band (1350 cm^{-1}) and G band (1580 cm^{-1})[42] suggests a high degree of carbonization in the Ru@TiC, which is conducive to charge transfer.[38] The electronic metal-support interactions between Ru NPs and TiC support can be verified by X-ray photoelectron spectroscopy (XPS). XPS survey spectrum (Figure S9, Supporting Information) confirms the presence of Ru, Ti, and C elements in the sample, which matches well with the EDS mapping. As shown in Figure 2b, the C 1s XPS spectrum of TiC can be deconvoluted into three peaks, the peaks around 282.2, 284.8, and 286.3 eV can be assigned to the C-Ti, C-C, and C-O bonds, respectively.[43,44] For the Ru@CNF sample, the spin orbitals of Ru 3d$_{5/2}$ and Ru 3d$_{3/2}$ were observed

at 280.8 and 285.5 eV, respectively, suggesting the metallic feature of Ru nanoparticles. Additional peaks located at 281.6 and 286.2 eV are attributed to the Ru $3d_{5/2}$ and Ru $3d_{3/2}$ orbits of Ru^{n+} species, respectively,[44] which may be caused by the inevitable surface oxidation. Interestingly, the slight negative shift of the Ru 3d peaks for Ru@TiC with respect to Ru@CNF suggests the occurrence of electron redistribution at the heterointerface of Ru NPs and TiC support. Figure 2c also shows the XPS spectra of the as-prepared samples in Ru 3p and Ti 2p regions. The Ru $3p_{3/2}$ spectrum of Ru@TiC is negatively shifted in comparison with that of Ru@CNF, further demonstrating the presence of electronic interactions between TiC and Ru.[16,44,45]

X-ray absorption spectroscopy (XAS), utilizing synchrotron radiation, was employed to investigate the detailed electronic structure and local bonding environment of the Ru@TiC sample. Figure 2d shows the Ru-K edge X-ray absorption near edge structure (XANES) spectra for Ru@TiC and Ru@CNF samples. In comparison to the Ru@CNF sample, the absorption edge of Ru@TiC exhibits a shift toward lower energy, revealing the lower valence states of Ru within the electrocatalyst. This observation is in accordance with the XPS results. Fourier transform function extended X-ray absorption fine structure (FT-EXAFS) indicates that the Ru-Ru bond paths for Ru@TiC and Ru@CNF are basically the same at 2.36 Å, which can be attributed to the backscattering of Ru-Ru coordination (Figure 2e).[46] In addition, Ti L-edge XANES spectra were carried out to investigate the local electronic structure changes of TiC support before and after Ru loading.[47,48] Figure 2f shows the soft-XANES Ti $L_{2,3}$-edge spectra for Ru@TiC and TiC. The peak at 457.6 eV in the L_3-edge corresponds to the transition from the $2p_{3/2}$ to the t_{2g} final state. The sharp t_{2g} resonance peak in the Ru@TiC sample suggests an increased valence state of Ti following Ru loading.[49,50] The results indicate that TiC supports can modulate the electronic structure of Ru NPs, triggering EMSI at the metal-support interface.[29,37,51]

2.2. Electrocatalytic Property

The electrochemical performance of the as-prepared catalysts (Ru@TiC, Ru@CNF, TiC, and CNF) and commercial Pt/C were evaluated in 1 M KOH with a three-electrode configuration. Linear sweep voltammetry (LSV) curves (with iR correction) were used to evaluate its catalytic performance, as shown in **Figure 3a**. Obviously, Ru@TiC electrocatalyst exhibits the best HER performance with a low overpotential of 25 mV at 10 mA cm^{-2}, superior to that of Pt/C (29 mV), Ru@CNF (40 mV), TiC (351 mV), and CNF (571 mV). In addition, Ru@TiC also demonstrates excellent catalytic performance at high current densities. As shown in Figure 3b, Ru@TiC electrode requires overpotentials of only 153 and 252 mV to reach the current densities of 500 (η_{500}) and 1000 mA cm^{-2} (η_{1000}), respectively, which is much lower than that of Pt/C (η_{500} = 242 mV, η_{1000} = 416 mV), Ru@CNF (η_{500} = 586 mV, η_{1000} = 1080 mV), and TiC (η_{500} = 721 mV, η_{1000} = 841 mV). Meanwhile, the kinetics of HER are assessed through Tafel plots of the as-synthesized electrocatalysts. As depicted in Figure 3c, Ru@TiC shows the lowest Tafel slope (30.6 mV dec^{-1}), which follows the Volmer-Tafel mechanism and is superior to Ru@CNF (60.1 mV dec^{-1}), TiC (185.7 mV dec^{-1}), and even comparable to commercial Pt/C (32.6 mV dec^{-1}). The mass activity of the noble metal-based catalysts was used to further assess the utilization efficiency (Figure 3d). Ru@TiC possesses the highest mass activity (8347 mA mg^{-1}), which is 6.4 times more than that of Pt/C (1296 mA mg^{-1}) and 8.3 times more than that of Ru@CNF (1007 mA mg^{-1}) at the potential of -0.15 V (vs RHE). In addition, the electrochemical active surface area (ECSA) of Ru@TiC and Ru@CNF was further estimated by the underpotential deposition of copper (Cu-UPD). As shown in Figure S10 (Supporting Information), the ECSA of Ru@TiC is calculated to be 63.6 m^2 g^{-1}, which is ≈2.4 times higher than Ru@CNF (26.6 m^2 g^{-1}). Furthermore, Figure S11a (Supporting Information) shows the ECSA-normalized polarization curves, in which Ru@TiC still possesses the superior catalytic performance. The superior intrinsic catalytic activity of Ru@TiC is further validated by its high turnover frequency (TOF), as demonstrated in Figure S11b (Supporting Information). The HER performance of Ru@TiC is comparable or even better than the previously reported noble metal-based electrocatalysts (Figure 3e; Table S1, Supporting Information). In addition, the reported thermal shock method can also be extended to the preparation of non-noble metal-based catalysts. As illustrated in Figures S12–S15 (Supporting Information), the uniformly dispersed non-noble metals@TiC catalysts show the enhanced HER performance.

The durability of electrocatalysts serves as a crucial criterion for evaluating their performance in the HER process. Figure 3f illustrates the multi-current step chronopotentiometric curves of Ru@TiC, where the current density is incremented from 100 mA cm^{-2} to 1000 mA cm^{-2} in steps of 100 mA cm^{-2} every 600 seconds. The initial drop and subsequent stabilization of potential with rising current density highlights the superior conductivity, mechanical stability, and mass transport efficiency of the self-supported Ru@TiC electrode.[2,4] Additionally, accelerated aging tests and long-term stability tests at high current density were conducted to evaluate the catalyst stability of Ru@TiC. As shown in Figure 3g, Ru@TiC shows negligible attenuation in HER activity after 5000 continuous cyclic voltammetry (CV) cycles. In addition, the chronopotentiometric measurement at a constant current density of 500 mA cm^{-2} illustrates that Ru@TiC can maintain the catalytic performance for at least 250 hours during alkaline HER process (Figure 3h). Various characterization techniques were utilized to assess the stability of the Ru@TiC electrocatalyst after the long-term duration measurements. XRD patterns of Ru@TiC show negligible alterations after HER in 1 M KOH (Figure S16, Supporting Information). Additionally, SEM images in Figure S17 (Supporting Information) show that the fibrous morphology of Ru@TiC is well preserved. TEM images in Figure S18 (Supporting Information) confirm that the Ru NPs remain uniformly dispersed on the nanofibers, demonstrating the excellent stability of the Ru@TiC electrocatalyst during long-term electrolysis process.

2.3. HER Performance of Ru@TiC in Alkaline Seawater

Direct seawater electrolysis is gaining increasing importance due to the scarcity of freshwater resources. To explore its suitability for such applications, we further evaluate the electrochemical corrosion behavior of TiC nanofibers by using electrochemical polarization curve in an alkaline seawater environment. As

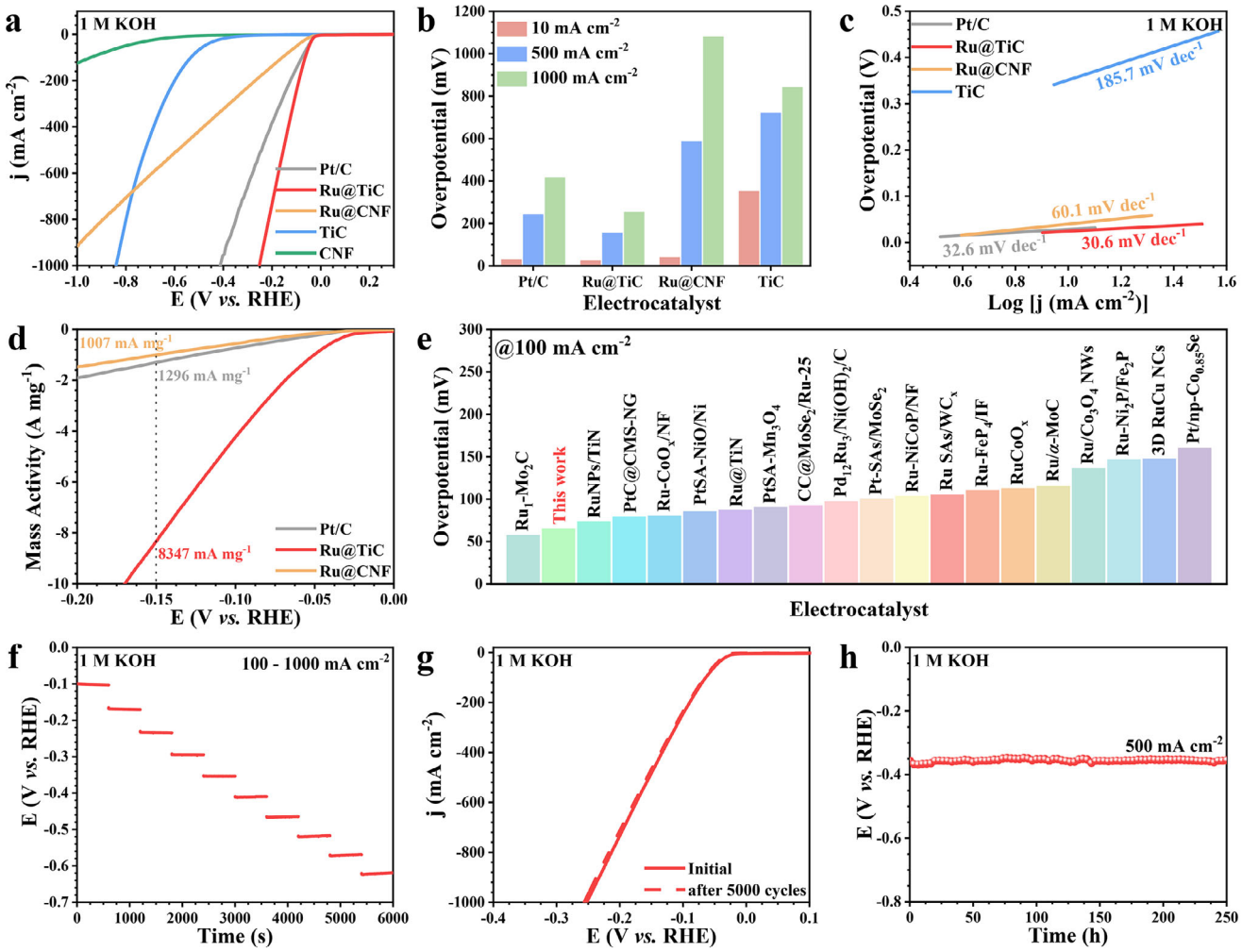

Figure 3. a) Polarization curves of Ru@TiC, Ru@CNF, TiC, CNF, and Pt/C in 1 M KOH. b) Overpotentials at current densities of 10, 500, and 1000 mA cm^{-2} of Ru@TiC, Ru@CNF, TiC, and Pt/C. c) Tafel plots of Ru@TiC, Ru@CNF, TiC, and Pt/C. d) Mass activity of Ru@TiC, Ru@CNF, and Pt/C. e) Overpotentials at the current density of 100 mA cm^{-2} for noble metal-based catalysts in 1 M KOH (more detailed comparisons can be seen in Table S1, Supporting Information). f) Chronopotentiometric responses of Ru@TiC at 100–1000 mA cm^{-2} with an increment of 100 mA cm^{-2} (without iR compensation). g) Polarization curves of the Ru@TiC before and after 5000 continuous CV scanning. h) Chronopotentiometric measurement of Ru@TiC at 500 mA cm^{-2} for 250 hours (without iR compensation).

illustrated in Figure S19 (Supporting Information), TiC exhibits outstanding corrosion resistance in alkaline seawater, with a corrosion current of only 1.65×10^{-5} A cm^{-2}, which is significantly lower than that of CNF (9.82×10^{-5} A cm^{-2}). This lower corrosion current demonstrates the superior corrosion resistance of TiC nanofibers, underscoring their potential applications in alkaline seawater environments.

Anticipating that catalyst activity might alter with increasing salt concentrations during seawater splitting,[52] the HER performance of the Ru@TiC electrocatalyst was evaluated using a three-electrode system in both alkaline saturated NaCl solution and alkaline natural seawater, as shown in **Figure** 4a,b. In alkaline seawater electrolyte, Ru@TiC achieves current densities of 100, 500, and 1000 mA cm^{-2} at the overpotentials of only 65, 156, and 268 mV, respectively. This performance is comparable to that in 1.0 M KOH (η_{100} = 64 mV, η_{500} = 153 mV, and η_{1000} = 252 mV), alkaline 0.5 M NaCl solution (η_{100} = 64 mV, η_{500} = 146 mV, and η_{1000} = 235 mV) and alkaline saturated NaCl solution (η_{100} = 64 mV, η_{500} = 143 mV, and η_{1000} = 220 mV). Furthermore, Figure 4c illustrates that the Tafel slopes for Ru@TiC in alkaline seawater, alkaline 0.5 M NaCl solution and alkaline saturated NaCl solution are 42.7, 30.7, and 23.9 mV dec^{-1}, respectively. The observed differences in saturated NaCl solution can be attributed to the enhanced conductivity of the solution following the introduction of a substantial amount of NaCl.[53,54] In addition, Ru@TiC catalyst also demonstrates remarkable stability, sustaining its performance for at least 250 hours at 500 mA cm^{-2} in both alkaline saturated NaCl solution (Figure S20, Supporting Information) and alkaline seawater (Figure 4d). Post-reaction characterization of the Ru@TiC catalyst in alkaline seawater confirmed its stability. As shown in Figure S21 (Supporting Information), XRD patterns reveal that the crystal phase of the catalyst remains largely unchanged. Additionally, SEM (Figure S22, Supporting Information) and TEM (Figure S23, Supporting

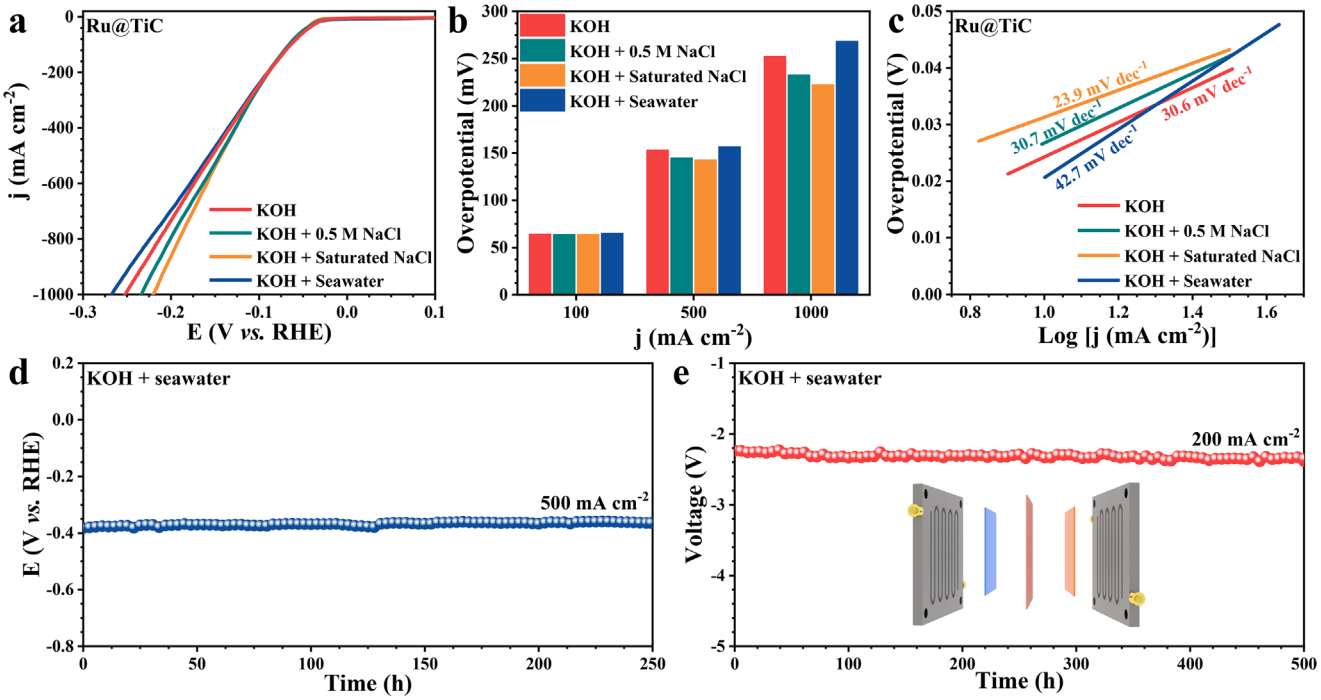

Figure 4. a) LSV polarization curves, b) overpotentials at current densities of 100, 500, and 1000 mA cm^{-2} and c) Tafel plots for Ru@TiC in different solutions. d) Chronopotentiometric measurements of Ru@TiC at 500 mA cm^{-2} for HER in alkaline seawater (without iR compensation). e) Operating voltage at constant 200 mA cm^{-2} in the AEMWE. Inset: the schematic diagram of an AEMWE.

Information) images confirm the preservation of the fibrous structure and uniform dispersion of Ru NPs. Furthermore, as depicted in Figure 4e, an alkaline anion-exchange membrane water electrolyzer (AEMWE) was constructed with Ru@TiC as the cathode and NiFeP/Ni_3S_2 nanosheet array as the anode.[10] Remarkably, the AEMWE can continuously operate steadily at current density of 200 mA cm^{-2} for over 500 hours with negligible changes in cell voltage, demonstrating its excellent electrochemical stability during seawater electrolysis. The aforementioned data highlight the stability of the Ru@TiC electrocatalyst in the complex seawater environment and underscore its significant potential for large-scale industrial seawater electrolysis.

2.4. Mechanism Exploration

Density functional theory (DFT) calculations were employed to elucidate the underlying regulation mechanism of the TiC substrate. Figure S24 (Supporting Information) shows the structural models of Ru (101) and Ru dispersed on TiC (200), denoted as Ru-TiC (200). To understand the interaction between Ru and TiC, the charge density difference distribution of Ru-TiC (200) was calculated (**Figure** 5a). At the interface, charge depletes on the TiC surface while charge accumulation occurs on the Ru surface, indicating strong interfacial interactions between Ru and TiC. From the Bader charge analysis, ≈0.29 |e| is transferred from TiC to Ru, which is in good agreement with the XPS and the XANES results. Figures 5b,c show the partial density of states (PDOS) of Ru and Ru-TiC (200), respectively. Notably, the d-band center of Ru shifts from -2.47 eV in Ru (101) to -2.76 eV in Ru-TiC (200). According to d-band theory, the downshift of the d-band center suggests a weakened adsorption between intermediates and Ru sites, thereby promoting the enhancement of HER activity.[55,56] As shown in Figure S25 (Supporting Information), the calculated absorption energies of $^*H$ on Ru (101) and Ru-TiC (200) are -4.12 and -4.01 eV, respectively, indicating the weaker $^*H$ adsorption for Ru-TiC (200). This difference is mainly attributed to the EMSI effect between Ru and TiC. Additionally, under the alkaline media, the adsorption energy of OH^- can also affect the performance of HER electrocatalysts.[57] As shown in Figure S26 (Supporting Information), Ru-TiC (200) exhibits a weak adsorption strength, thereby facilitating the desorption of OH^- groups from the electrocatalyst and thus creating a more favorable catalytic environment for water reduction. Furthermore, the change in Gibbs free energy for the overall alkaline HER process is depicted in Figure 5d. Ru-TiC (200) demonstrates lower energy barriers during HER process compared with Ru (101). Thus, the EMSI between Ru and TiC optimizes the adsorption intermediates of HER process, thereby enhancing the activity for catalytic hydrogen evolution in alkaline electrolytes. Considering the high concentration of Cl^- in the seawater environment, we employed the adsorption energy of Cl^- to evaluate the corrosion resistance of the electrocatalysts. As demonstrated in Figure S27 (Supporting Information), Ru-TiC (200) exhibits a modest adsorption strength for Cl^-, indicating the possibility of enhanced corrosion resistance.

In order to deeply elucidate the origin of enhanced HER catalytic performance, a series of experiments were carried out. Hydrogen temperature-programmed desorption (H_2-TPD) was used to investigate hydrogen desorption capacity of the

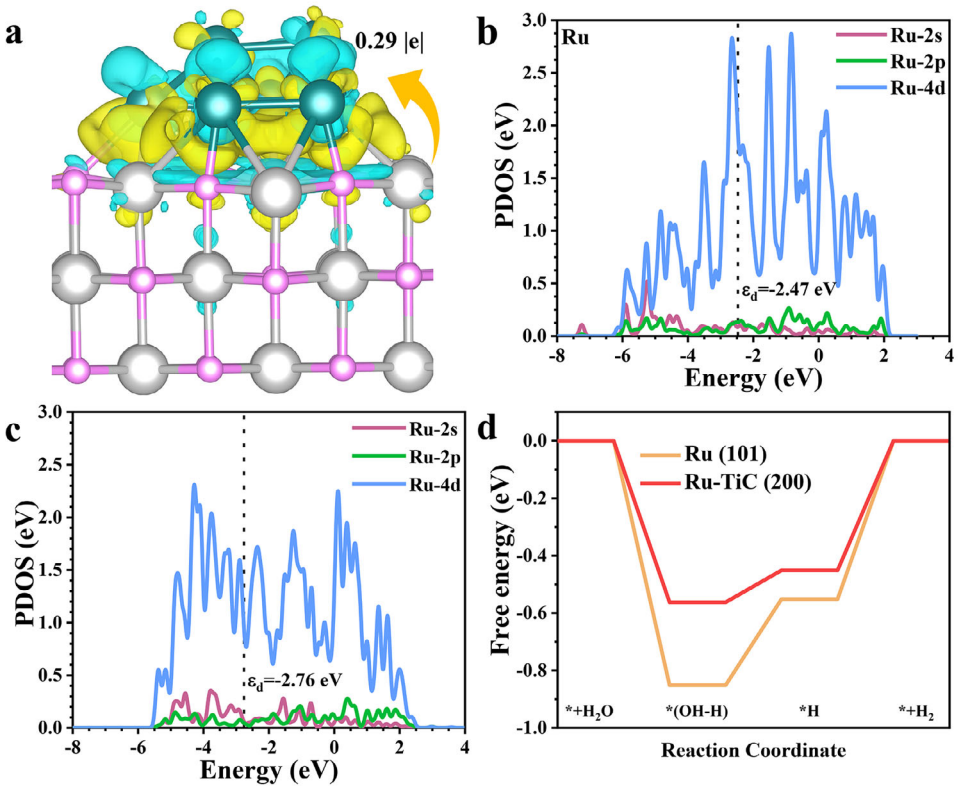

Figure 5. a) Differential charge density distribution of Ru-TiC (200). The yellow and blue zones represent the charge accumulation and depletion, respectively. The partial density of states for b) Ru (101) and c) Ru-TiC (200), the Fermi energy level is set to 0. d) Gibbs free energy diagram of the alkaline HER process.

catalyst. As shown in Figure S28 (Supporting Information), the H_2-TPD profile of Ru@TiC presents a lower H_2 desorption temperature than TiC, suggesting that the electronic metal-support interactions between Ru NPs and TiC support can promote the activation of H.[16] Moreover, **Figure 6**a displays the H_2-hydrogen temperature-programmed reduction (H_2-TPR) profiles. For Ru@TiC, the peak located at 167 °C can be attributed to the reduction peak of surface Ru species. Interestingly, the main reduction peak of Ru@TiC appears at 433 °C, which is significantly lower than the 553 °C peak of pure TiC. This shift is attributed to the supplementary reduction effect induced by active hydrogen spillover from the Ru NPs.[58,59] These results indicate the presence of electronic metal-support interactions between Ru NPs and TiC support, which triggers hydrogen spillover effects between them.

In addition, the hydrogen desorption kinetics could be discerned through electrochemical impedance spectroscopy (EIS) under varying overpotentials (Figure S29, Supporting Information). It is recognized that integrating the C_φ versus η plot allows for the quantification of the substantial quantity of adsorbed hydrogen on the catalyst surface during the HER,[46,60] which is indicative of the hydrogen adsorption charge (Q_H). Notably, the Q_H value for Ru@TiC is approximately three times greater than that for Ru@CNF, indicating a significantly enhanced adsorbed hydrogen (H^*) coverage on the Ru@TiC surface.[61] Additionally, the hydrogen binding energy (HBE) was determined using the CV technique within a potential window of 0-0.5 V (Figure S30, Supporting Information), where the HBE value serves as a crucial indicator for assessing HER activities.[18,57] Compared with Ru@CNF, it is evident that the hydrogen underpotential deposition (H_{UPD}) desorption peak for Ru@TiC shifts toward a negative potential, confirming the favorable hydrogen desorption kinetics. The appropriately diminished HBE is advantageous for hydrogen recombination during the HER process. Furthermore, the hydrogen desorption kinetics can be estimated through the dependence of the desorption peak position on various CV scan rates (Figure S31, Supporting Information). As shown in Figure 6b, the slope order of Ru@TiC (1.46×10^{-3}) < Ru@CNF (1.97×10^{-3}), indicating enhanced hydrogen desorption kinetics. The accelerated hydrogen desorption kinetics observed for Ru@TiC may be ascribed to the hydrogen spillover effect.[46,60,62]

Meanwhile, in situ Raman spectroscopy was employed to examine the dynamic reaction process of Ru@TiC. Raman spectrum of Ru@TiC displays a pronounced peak for interfacial water within the range of 3000–3600 cm^{-1} (Figure S32, Supporting Information).[18,63] The peak intensity diminishes with increasing voltage, revealing effective water dissociation on the Ru@TiC surface. To further gain insight into the active site, deactivation experiments utilizing potassium thiocyanate (KSCN) as poison were conducted to ascertain if Ru NPs are the primary catalytic sites. The SCN^- ion can adsorb onto the Ru NPs surfaces, leading to a reduction in HER activity.[64,65] As shown in Figure S33 (Supporting Information), the HER activity of Ru@TiC significantly deteriorates upon SCN^- ion poisoning, suggesting that Ru NPs

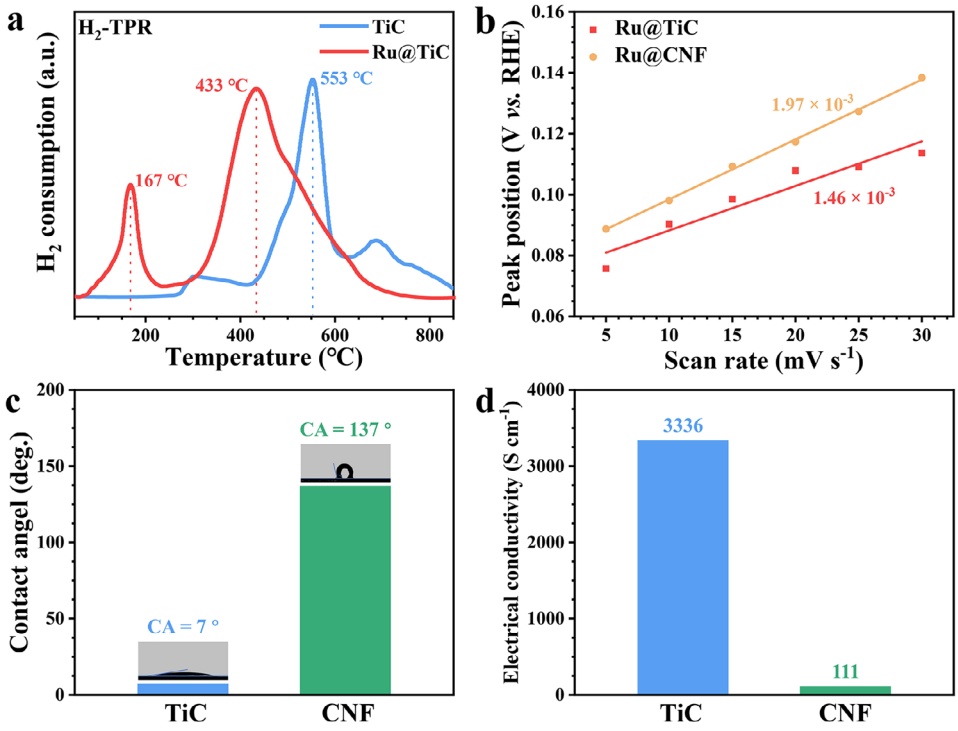

Figure 6. a) H_2-TPR profiles of Ru@TiC and TiC. b) Plots of hydrogen desorption peak position versus scan rates of Ru@TiC and Ru@CNF. Water contact angles of c) TiC nanofiber mat and CNF mat. d) Electrical conductivity of TiC mat and CNF mat.

are the main active sites for HER. Based on the above results, the enhanced catalytic performance for the HER can be attributed to the EMSI between Ru NPs and TiC support. This interaction triggers hydrogen spillover phenomenon, which optimizes the hydrogen desorption kinetics and markedly enhances HER efficiency.

In addition to the EMSI between Ru NPs and TiC nanofibers, the structural differences between TiC and CNF supports may also exert additional influences on the electrocatalytic performance of HER. Figure 6c shows the water contact angle (CA) images of the TiC and CNF mats. Compared with the CNF supports (137.5°), TiC exhibits remarkable superhydrophilicity (< 10°), which plays a key role in enhancing HER performance by improving electrolyte contact and facilitating mass transport.[66,67] Moreover, conductivity is a critical factor for electrocatalytic system. As illustrated in Figure 6d, TiC exhibits metallic characteristic with electrical conductivity of 3336 S cm^{-1}, ≈30 times greater than that of CNF mat (111 S cm^{-1}). The high electrical conductivity of the functionalized support can facilitate rapid electron transfer between the interface of Ru NPs and TiC support, thereby further enhancing the catalytic activity of Ru@TiC.[68,69]

3. Conclusion

In conclusion, we developed simple methods combining electrospinning and thermal shock technology to disperse Ru NPs onto conductive TiC nanofibers. DFT calculations reveal that TiC induces charge transfer from TiC to Ru, resulting in the downshift of the d-band center of interfacial Ru sites, consequently facilitating the desorption of $^*H$ at the Ru-TiC interface. The experimental results further indicate that the EMSI at the Ru-TiC interface may trigger hydrogen spillover effect, thereby improve hydrogen evolution performance. Consequently, Ru@TiC exhibits outstanding HER activity in alkaline seawater condition, requiring low overpotentials of only 65 mV to reach the current density of 100 mA cm^{-2}, and demonstrates excellent stability at 500 mA cm^{-2} for over 250 hours. Moreover, it operated stably for at least 500 hours at 200 mA cm^{-2} in an AEM electrolyzer under alkaline seawater conditions. This study highlights the potential of robust TiC supports for fabricating durable electrocatalysts to enhance hydrogen production through electronic metal-support interaction.

Supporting Information

Supporting Information is available from the Wiley Online Library or from the author.

Acknowledgements

This study was financially supported by the National Key Research and Development Program of China (2022YFB4004400), National Natural Science Foundation of China (Nos. 52271095, 51871057, and 22209088), Natural Science Foundation of Fujian (2022J01946), Taishan Scholar Program (tsqn202103058), Qingdao New Energy Shandong Laboratory Open Project (QNESL OP202302), and the Open Funds of the State Key Laboratory of Electroanalytical Chemistry (SKLEAC202310). The authors acknowledge the support of the NSRL (Beamlines MCD-A and MCD-B, Soochow Beamline for Energy Materials) in the XAS experiments.

Conflict of Interest

The authors declare no conflict of interest.

Data Availability Statement

The data that support the findings of this study are available from the corresponding author upon reasonable request.

Keywords

alkaline seawater electrolysis, desorption kinetics, electronic metal-support interactions, ruthenium nanoparticles, titanium carbide nanofibers

Received: December 10, 2024
Revised: February 22, 2025
Published online:

[1] Z. W. Seh, J. Kibsgaard, C. F. Dickens, I. Chorkendorff, J. K. Nørskov, T. F. Jaramillo, *Science* **2017**, *355*, eaad4998.
[2] Z. Wang, H. Liu, R. Ge, X. Ren, J. Ren, D. Yang, L. Zhang, X. Sun, *ACS Catal.* **2018**, *8*, 2236.
[3] X. Li, T. Wu, N. Li, S. Zhang, W. Chang, J. Chi, X. Liu, L. Wang, *Adv. Funct. Mater.* **2024**, *34*, 2400734.
[4] J. Sun, W. Xu, C. Lv, L. Zhang, M. Shakouri, Y. Peng, Q. Wang, X. Yang, D. Yuan, M. Huang, Y. Hu, D. Yang, L. Zhang, *Appl. Catal. B* **2021**, *286*, 119882.
[5] D. Yuan, Z. Hu, Z. Chen, J. Liu, J. Sun, Y. Song, S. Dong, L. Zhang, *J. Phys. Chem. Lett.* **2024**, *15*, 3486.
[6] H. Hu, X. Wang, J. P. Attfield, M. Yang, *Chem. Soc. Rev.* **2024**, *53*, 163.
[7] Y. Song, M. Sun, S. Zhang, X. Zhang, P. Yi, J. Liu, B. Huang, M. Huang, L. Zhang, *Adv. Funct. Mater.* **2023**, *33*, 2214081.
[8] Y. Liu, Y. Wang, P. Fornasiero, G. Tian, P. Strasser, X.-Y. Yang, *Angew. Chem., Int. Ed.* **2024**, *63*, 202412087.
[9] H. Chen, Y.-Q. Wang, R. Ding, Z.-W. Zeng, B.-W. Liu, F.-R. Zeng, Y.-Z. Wang, H.-B. Zhao, *Matter* **2024**, *7*, 3189.
[10] Y. Song, X. Zhang, Z. Xiao, Y. Wang, P. Yi, M. Huang, L. Zhang, *Appl. Catal. B* **2024**, *352*, 124028.
[11] L. Yu, Q. Zhu, S. Song, B. McElhenny, D. Wang, C. Wu, Z. Qin, J. Bao, Y. Yu, S. Chen, Z. Ren, *Nat. Commun.* **2019**, *10*, 5106.
[12] H. Fei, R. Liu, T. Liu, M. Ju, J. Lei, Z. Wang, S. Wang, Y. Zhang, W. Chen, Z. Wu, M. Ni, J. Wang, *Adv. Mater.* **2024**, *36*, 2309211.
[13] Y. Zheng, Y. Jiao, A. Vasileff, S. Z. Qiao, *Angew. Chem., Int. Ed.* **2018**, *57*, 7568.
[14] N. Mahmood, Y. Yao, J.-W. Zhang, L. Pan, X. Zhang, J.-J. Zou, *Adv. Sci.* **2018**, *5*, 1700464.
[15] Y. Zheng, Y. Jiao, Y. Zhu, L. H. Li, Y. Han, Y. Chen, M. Jaroniec, S.-Z. Qiao, *J. Am. Chem. Soc.* **2016**, *138*, 16174.
[16] X. Wang, X. Yang, G. Pei, J. Yang, J. Liu, F. Zhao, F. Jin, W. Jiang, H. Ben, L. Zhang, *Carbon Energy* **2023**, *6*, e391.
[17] S. Zhao, S.-F. Hung, L. Deng, W.-J. Zeng, T. Xiao, S. Li, C.-H. Kuo, H.-Y. Chen, F. Hu, S. Peng, *Nat. Commun.* **2024**, *15*, 2728.
[18] Z. Wu, Q. Li, G. Xu, W. Jin, W. Xiao, Z. Li, T. Ma, S. Feng, L. Wang, *Adv. Mater.* **2024**, *36*, 2311018.
[19] H. Chen, X. Ai, W. Liu, Z. Xie, W. Feng, W. Chen, X. Zou, *Angew. Chem., Int. Ed.* **2019**, *58*, 11409.
[20] Q. Huang, W. Yang, Y. Yan, S. Xie, A. Yu, T. Xu, Y. Zhao, P. Peng, F.-F. Li, *Adv. Funct. Mater.* **2024**, *34*, 2409406.
[21] Y. Cong, L. Chen, M. Liu, H. Wang, L. Zhang, Q. Zhao, C. Li, *Chem. Eng. J.* **2024**, *495*, 153433.
[22] D. H. Kweon, M. S. Okyay, S.-J. Kim, J.-P. Jeon, H.-J. Noh, N. Park, J. Mahmood, J.-B. Baek, *Nat. Commun.* **2020**, *11*, 1278.
[23] C. T. Campbell, *Nat. Chem.* **2012**, *4*, 597.
[24] J. Yang, W. Li, D. Wang, Y. Li, *Adv. Mater.* **2020**, *32*, 2003300.
[25] M. Smiljanić, S. Panić, M. Bele, F. Ruiz-Zepeda, L. Pavko, L. Gašparič, A. Kokalj, M. Gaberšček, N. Hodnik, *ACS Catal.* **2022**, *12*, 13021.
[26] X. Wang, Y. Zhang, J. Li, G. Liu, M. Gao, S. Ren, B. Liu, L. Zhang, G. Han, J. Yu, H. Zhao, F. Rosei, *Small Methods* **2022**, *6*, 2101470.
[27] E. R. Hamo, R. K. Singh, J. C. Douglin, S. Chen, M. B. Hassine, E. Carbo-Argibay, S. Lu, H. Wang, P. J. Ferreira, B. A. Rosen, D. R. Dekel, *ACS Catal.* **2021**, *11*, 932.
[28] Y. Yang, D. Wu, R. Li, P. Rao, J. Li, P. Deng, J. Luo, W. Huang, Q. Chen, Z. Kang, Y. Shen, X. Tian, *Appl. Catal. B* **2022**, *317*, 121796.
[29] Y. Feng, Y. Xie, Y. Yu, Y. Chen, Q. Liu, H. Bao, F. Luo, S. Pan, Z. Yang, *Angew. Chem., Int. Ed.* **2024**, *64*, 202413417.
[30] C. Li, S. H. Kim, H. Y. Lim, Q. Sun, Y. Jiang, H.-J. Noh, S.-J. Kim, J. Baek, S. K. Kwak, J.-B. Baek, *Adv. Mater.* **2023**, *35*, 2301369.
[31] Y. Liu, T. G. Kelly, J. G. Chen, W. E. Mustain, *ACS Catal.* **2013**, *3*, 1184.
[32] Q. Gao, W. Zhang, Z. Shi, L. Yang, Y. Tang, *Adv. Mater.* **2019**, *31*, 1802880.
[33] Y. Cho, J. Park, W.-G. Lee, J. Park, K. Shin, I. Song, G. Lee, J. Cho, S. J. Kang, Y. Kim, M.-J. Baek, D. W. Lee, *Adv. Funct. Mater.* **2023**, *33*, 2213853.
[34] Y. C. Kimmel, L. Yang, T. G. Kelly, S. A. Rykov, J. G. Chen, *J. Catal.* **2014**, *312*, 216.
[35] T. W. van Deelen, C. Hernández Mejía, K. P. de Jong, *Nat. Catal.* **2019**, *2*, 955.
[36] J. Dong, Q. Fu, Z. Jiang, B. Mei, X. Bao, *J. Am. Chem. Soc.* **2018**, *140*, 13808.
[37] M. Xu, M. Peng, H. Tang, W. Zhou, B. Qiao, D. Ma, *J. Am. Chem. Soc.* **2024**, *146*, 2290.
[38] X. Xia, J. Zhan, Y. Zhong, X. Wang, J. Tu, H. J. Fan, *Small* **2017**, *13*, 1602742.
[39] X. Zhang, W. Yuan, Y. Yang, Y. Chen, Z. Tang, C. Wang, Y. Yuan, Y. Ye, Y. Wu, Y. Tang, *Small* **2020**, *16*, 2005998.
[40] Z. Yao, X. Xia, D. Xie, Y. Wang, C.-a. Zhou, S. Liu, S. Deng, X. Wang, J. Tu, *Adv. Funct. Mater.* **2018**, *28*, 1802756.
[41] Q. Dong, S. Ma, J. Zhu, F. Yue, Y. Geng, J. Zheng, Y. Ge, C. Fan, H. Zhang, M. Xiang, Q. Zhu, *Adv. Funct. Mater.* **2023**, *33*, 2210665.
[42] L. Liu, Q. He, S. Dong, M. Wang, Y. Song, H. Diao, D. Yuan, *J. Colloid Interface Sci.* **2024**, *666*, 35.
[43] L.-Å. Näslund, I. Persson, *Appl. Surf. Sci.* **2022**, *593*, 153442.
[44] J. Zhao, R. Urrego-Ortiz, N. Liao, F. Calle-Vallejo, J. Luo, *Nat. Commun.* **2024**, *15*, 6391.
[45] Z. Jiang, S. Song, X. Zheng, X. Liang, Z. Li, H. Gu, Z. Li, Y. Wang, S. Liu, W. Chen, D. Wang, Y. Li, *J. Am. Chem. Soc.* **2022**, *144*, 19619.
[46] Y. Chen, Y. Liu, L. Li, T. Sakthivel, Z. Guo, Z. Dai, *Adv. Funct. Mater.* **2024**, *34*, 2401452.
[47] J. T. Lau, J. Rittmann, V. Zamudio-Bayer, M. Vogel, K. Hirsch, P. Klar, F. Lofink, T. Möller, B. V. Issendorff, *Phys. Rev. Lett.* **2008**, *101*, 153401.
[48] P. Zhang, L. Li, D. Nordlund, H. Chen, L. Fan, B. Zhang, X. Sheng, Q. Daniel, L. Sun, *Nat. Commun.* **2018**, *9*, 381.
[49] J.-W. Wu, C.-H. Chen, C.-J. Lin, K. Kumar, Y.-R. Lu, S. Ya Hsuan Liou, S.-Y. Chen, D.-H. Wei, C. Li Dong, C.-L. Chen, *Appl. Surf. Sci.* **2020**, *527*, 146844.
[50] C. L. Chen, C.-L. Dong, C.-H. Chen, J.-W. Wu, Y.-R. Lu, C.-J. Lin, S. Ya Hsuan Liou, C.-M. Tseng, K. Kumar, D.-H. Wei, J. Guo, W.-C. Chou, M.-K. Wu, *Phys. Chem. Chem. Phys.* **2015**, *17*, 22064.
[51] J. Yang, W.-H. Li, S. Tan, K. Xu, Y. Wang, D. Wang, Y. Li, *Angew. Chem., Int. Ed.* **2021**, *60*, 19085.
[52] X. Xu, Y. Lu, J. Shi, X. Hao, Z. Ma, K. Yang, T. Zhang, C. Li, D. Zhang, X. Huang, Y. He, *Nat. Commun.* **2023**, *14*, 7708.
[53] H. J. Song, H. Yoon, B. Ju, D.-Y. Lee, D.-W. Kim, *ACS Catal.* **2020**, *10*, 702.

[54] S. Carbone, F. Proietto, F. Bonafede, R. L. Oliveri, B. Patella, F. Ganci, G. Aiello, P. Mandin, M. Kim, M. Scopelliti, R. Inguanta, *Electrochim. Acta* **2023**, *467*, 143120.
[55] X. Fan, C. Liu, M. Wu, B. Gao, L. Zheng, Y. Zhang, H. Zhang, Q. Gao, X. Cao, Y. Tang, *Appl. Catal. B* **2022**, *318*, 121867.
[56] Y. Li, Z. Dou, Y. Pan, H. Zhao, L. Yao, Q. Wang, C. Zhang, Z. Yue, Z. Zou, Q. Cheng, H. Yang, *Nano Lett.* **2024**, *24*, 5705.
[57] X. Lin, W. Hu, J. Xu, X. Liu, W. Jiang, X. Ma, D. He, Z. Wang, W. Li, L.-M. Yang, H. Zhou, Y. Wu, *J. Am. Chem. Soc.* **2024**, *146*, 4883.
[58] M. Xiong, Z. Gao, P. Zhao, G. Wang, W. Yan, S. Xing, P. Wang, J. Ma, Z. Jiang, X. Liu, J. Ma, J. Xu, Y. Qin, *Nat. Commun.* **2020**, *11*, 4773.
[59] H. Shen, H. Li, Z. Yang, C. Li, *Green Energy Environ.* **2022**, *7*, 1161.
[60] C. Li, C. Tian, H. Tang, M. Liu, L. Zheng, F. Huang, G.-R. Li, Q. Li, *ACS Energy Lett.* **2023**, *8*, 5161.
[61] X. Wang, Y. He, Q. Zhang, S. Sun, Z. Li, Z. Cai, C. Yang, M. Yue, M. Zhang, H. Wang, A. Farouk, M. S. Hamdy, J. Hu, X. Sun, B. Tang, *ACS Mater. Lett.* **2024**, *6*, 3970.
[62] Z. Zhao, J. Sun, X. Li, S. Qin, C. Li, Z. Zhang, Z. Li, X. Meng, *Nat. Commun.* **2024**, *15*, 7475.
[63] Q. Li, F. Huang, S. Li, H. Zhang, X.-Y. Yu, *Small* **2022**, *18*, 2104323.
[64] X. Chen, C. Chen, M. M. Amjad, D. Sun, B. Sun, K. Zhang, *Appl. Catal. B* **2024**, *344*, 123644.
[65] K. Wang, J. Cao, X. Yang, X. Sang, S. Yao, R. Xiang, B. Yang, Z. Li, T. O'Carroll, Q. Zhang, L. Lei, G. Wu, Y. Hou, *Adv. Funct. Mater.* **2023**, *33*, 2212321.
[66] L. Zhang, H. Hu, C. Sun, D. Xiao, H.-T. Wang, Y. Xiao, S. Zhao, K. H. Chen, W.-X. Lin, Y.-C. Shao, X. Wang, C.-W. Pao, L. Han, *Nat. Commun.* **2024**, *15*, 7179.
[67] H. Sun, L. Li, M. Humayun, H. Zhang, Y. Bo, X. Ao, X. Xu, K. Chen, K. Ostrikov, K. Huo, W. Zhang, C. Wang, Y. Xiong, *Appl. Catal. B* **2022**, *305*, 121088.
[68] Y. P. Zhu, C. Guo, Y. Zheng, S.-Z. Qiao, *Acc. Chem. Res.* **2017**, *50*, 915.
[69] X. Zhao, H. Zhang, Y. Yan, J. Cao, X. Li, S. Zhou, Z. Peng, J. Zeng, *Angew. Chem., Int. Ed.* **2017**, *56*, 328.